On quantitativeness of diffraction-limited quantitative phase imaging

Cite as: APL Photon. 9, 126111 (2024); doi: 10.1063/5.0232405
Submitted: 7 August 2024 • Accepted: 18 November 2024 •
Published Online: 11 December 2024

Zdeněk Bouchal,[1] Petr Bouchal,[2,3,a)] Tereza Chmelíková,[3] and Jaromír Fiurášek[1]

AFFILIATIONS

[1] Department of Optics, Palacký University, 17. listopadu 1192/12, 771 46 Olomouc, Czech Republic
[2] Institute of Physical Engineering, Faculty of Mechanical Engineering, Brno University of Technology, Technická 2, 616 69 Brno, Czech Republic
[3] Central European Institute of Technology, Brno University of Technology, Purkyňova 656/123, 612 00 Brno, Czech Republic

[a)] **Author to whom correspondence should be addressed:** petr.bouchal@ceitec.vutbr.cz

ABSTRACT

Quantitative phase imaging (QPI) has advanced by accurately quantifying phase shifts caused by weakly absorbing biological and artificial structures. Despite extensive research, the diffraction limits of QPI have not been established and examined. Hence, it remains unclear whether diffraction-affected QPI provides reliable quantification or merely visualizes phase objects, similar to phase contrast methods. Here, we develop a general diffraction phase imaging theory and show that it is intrinsically connected with Rayleigh's resolution theory. Our approach reveals the entanglement of phases under restoration, imposing diffraction bounds on spatial phase resolution and, unexpectedly, on phase accuracy. We prove that the phase accuracy depends on the size, shape, and absorption of objects forming the sample and significantly declines if the object size approaches the Rayleigh limit (a relative phase error of −16% for an Airy disk-sized object with low phase shift). We show that the phase accuracy limits can be enhanced at the cost of deteriorated phase resolution by attenuating the sample background light. The QPI diffraction limits are thoroughly examined in experiments with certified phase targets and biological cells. The study's relevance is underscored by results showing that the phase accuracy of some structures is lost (a relative phase error of −40%) even though they are spatially resolved (a phase visibility of 0.5). A reliable procedure is used to estimate phase errors in given experimental conditions, opening the way to mitigate errors' impact through data post-processing. Finally, the phase accuracy enhancement in super-resolution QPI is discovered, which has not been previously reported.

I. INTRODUCTION

Phase contrast and quantitative phase imaging (QPI) are milestones in developing optical microscopy, significantly impacting life and material sciences. Phase contrast imaging transforms phase variations induced by transparent samples into intensity variations, making subtle changes in refractive index visible without staining or labeling.[1] It highlights sample structures that are challenging to distinguish under traditional bright-field microscopy. The QPI goes a step further by visualizing phase shifts and quantifying them.[2,3] Phase shifts are measures of the sample optical path variations, enabling cellular growth monitoring or the optical weighing of cells through dry mass reconstructions. This quantitative approach is valuable in biology and biomedicine, providing insights into dynamic processes and morphological changes at the microscopic level.[4] However, the QPI extends beyond biophotonics and also allows for reconstructing a geometric phase.[5,6] In polymer liquid crystals, the geometric phase is modulated by changes in their molecular alignment, which transforms the polarization and shapes the wavefront of incident light.[7] Similarly, the orientation and shape of nanoantennas in plasmonic metasurfaces control the geometric phase and manipulate light.[8–10] The high optical performance of QPI is essential for the correct interpretation of phase measurements throughout the applications, allowing artifact-free examination of cellular structures or diagnostics of modern optical components.[11,12] The QPI optical performance relies on various factors, including the principles of phase reconstruction, the spatial coherence of illumination, the implementation of experiments, and

data processing algorithms, all of which have been recently examined by thorough numerical simulations based on the discrete dipole approximation.[13]

Although all QPI methods use interference-modulated intensity to restore phase images, the experimental implementations can be highly diverse. In widely used interferometric systems adapted to imaging, called holographic microscopes, the sample phase information carried by the sample field is compared with the known reference phase. Double-path and common-path holographic configurations have been developed to obtain the reference phase, each existing in several designs. In double-path QPI, the reference phase is sample-independent. The distinct sample and reference paths enable spatial phase shifting and single-shot phase reconstruction, thereby allowing the investigation of dynamic phenomena. Digital holographic microscopy,[14] Hilbert microscopy,[15] and optical quadrature microscopy[16] are typical representatives of the double-path configuration. The need for high robustness led to the common-path QPI, spatially filtering the reference wave out of the sample light. The phase reconstruction then requires temporal phase shifting with repeated recording of holograms.[17] This approach was used in Fourier phase microscopy,[18] diffraction phase microscopy,[19] and spatial light interference microscopy (SLIM).[20] Single-shot phase reconstruction was advantageously demonstrated in a robust common-path setup of geometric-phase microscopy based on polarization light coding.[21]

Attention was also focused on light coherence in QPI experiments. Simple systems operating with laser light are prone to speckle noise, and the definition of spatial resolution for coherent light is not consistently standardized within the imaging community.[22] Reducing spatial coherence mitigates the effects of coherent noise. Coherence-controlled QPI platforms using light self-correlation were developed,[23,24] enhancing spatial resolution and enabling imaging through turbid media thanks to coherence gating.[25] Broadband QPI with low temporal coherence light was also demonstrated,[26,27] and the white light phase was introduced and examined.[28] Considerable effort was devoted to optical QPI models, which become challenging under partially coherent illumination.[29,30] As the dependence of the partially coherent field on the sample parameters is nonlinear, approaches were proposed to linearize the imaging, assuming a weak sample.[31] The QPI was also described by the 3D coherent transfer function, which reveals the dependence of spatial frequency passband on the coherence properties of the source.[32] The precision of measurements depending on system inaccuracies was tested,[33] and fundamental QPI bounds based on the Cramér–Rao inequality were investigated for noisy data from coherent phase microscopy.[34] Efforts to improve QPI performance have led to the development of super-resolution techniques[35–39] and reconstruction algorithms incorporating machine learning.[40]

Over the past two decades, QPI has advanced significantly in system design, experimental implementation, and digital support. However, less attention has been given to evaluating the QPI optical performance in established techniques, making it challenging to select the most suitable method for specific applications. A newly published study addressed this issue by comparing the optical performance of eight different QPI configurations using a developed numerical toolbox.[13] Despite advances in numerical simulations, the QPI research still lacks a unifying concept with a clear optical insight into phase image formation and a strategy for assessing its optical performance. In particular, three key issues remain unaddressed: (i) a comprehensive diffraction QPI theory has not been developed, (ii) the diffraction limits of QPI have not been established, and (iii) the phase accuracy has not been systematically studied, so it is unclear how it relates to QPI principles, light coherence, and the optical properties of the imaged objects. This study introduces a diffraction and coherence QPI theory based on sample modeling, in which phase objects forming the observed sample are associated mathematically with their binarized amplitude replicas. The used approach demonstrates that the phase and amplitude images are intrinsically connected. The diffraction limitations of QPI are established for optical performance metrics, namely, for phase accuracy and spatial phase resolution assessed by phase visibility. The diffraction limits of phase imaging are estimated theoretically in relation to the Rayleigh resolution criterion and demonstrated experimentally with quantitative phase resolution targets and biological cells. The dependence of the phase accuracy and visibility on the object phase stroke, partial light coherence, and optical aberrations are investigated in the supplementary material. The deployment of the proposed concept in different QPI modes, including super-resolution modality, is also discussed.

II. MATERIALS AND METHODS

A. Description of diffraction and coherence effects in QPI

The theoretical QPI model is developed for thin samples consisting of weakly absorbing objects (e.g., biological cells) changing the optical path and, thus, the dynamic phase of light. The restoration of the sample phase is considered in a two-path holographic configuration, providing an independent reference phase. The examined holographic QPI is shown in Fig. 1(a). Light from a monochromatic spatially incoherent source LS is directed into the sample and reference paths, providing Köhler illumination of the observed sample S and reference sample RS with coordinates $\boldsymbol{r}_S = (x_S, y_S)$ and $\boldsymbol{r}_R = (x_R, y_R)$, respectively. Because the illumination uses a spatially incoherent source, its complex amplitude u oscillates randomly. The spatial correlation of light between points $\boldsymbol{r}_S$ and $\boldsymbol{r}_R$ varies with their mutual distance and can be expressed by averaging as $\Gamma(\boldsymbol{r}_S - \boldsymbol{r}_R) = \langle u(\boldsymbol{r}_S)u^*(\boldsymbol{r}_R)\rangle$. A full correlation occurs only at such points of the observed and reference samples $\boldsymbol{r}_S$ and $\boldsymbol{r}_R$, which are images of the same point of the collector field diaphragm. At each point of the object planes in the sample and reference paths, the complex amplitude of the incident light is affected by the sample transmission functions $T_S(\boldsymbol{r}_S)$ and $T_R(\boldsymbol{r}_R)$, respectively. These functions are complex, meaning the samples change the light amplitude and phase. The light scattered at the sample point $\boldsymbol{r}_S$ with a complex amplitude $u_S(\boldsymbol{r}_S)T_S(\boldsymbol{r}_S)$ is captured by a microscope consisting of a microscope objective MO and a tube lens TL. The light from the point $\boldsymbol{r}_S$ is distributed across the image plane with coordinates $\boldsymbol{r}' = (x', y')$ as $u_S(\boldsymbol{r}_S)T_S(\boldsymbol{r}_S)H(\boldsymbol{r}', \boldsymbol{r}_S)$, where H is the complex impulse response of the microscope. By integrating the contributions of all points, the resulting complex amplitude $U_S(\boldsymbol{r}')$ from the observed sample is obtained. Since identical microscopes are used in both interferometric paths, the light from the point $\boldsymbol{r}_R$ is determined by the same complex impulse response H at the image plane,

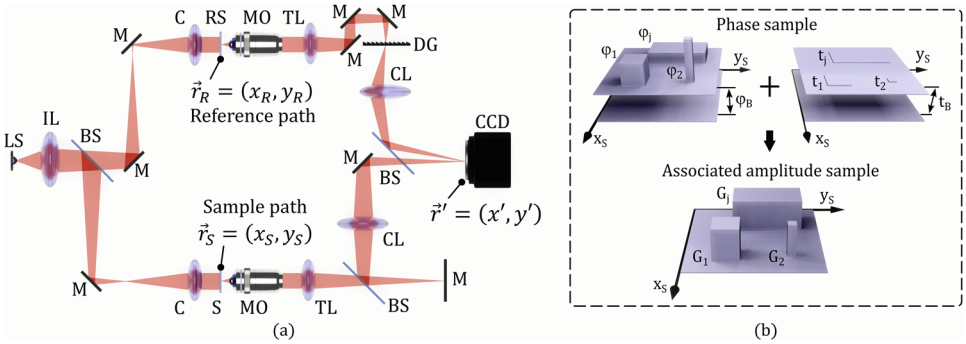

FIG. 1. Graphics supporting the calculation model. (a) Optical layout of the holographic QPI with independent sample and reference paths: LS: light source, IL: illumination lens, BS: beam splitters, M: mirrors, C: condensers, S: sample, RS: reference sample, DG: diffraction grating, MO: microscope objectives, TL: tube lenses, and CL: camera lens. (b) Phase sample composed of J weakly absorbing objects that have transmittances t_j and impose phases φ_j on light passing through the areas S_j, $j = 1, J$, and are embedded in the sample background with the transmittance t_B and phase φ_B. Artificially created amplitude sample composed of binary amplitude replicas of phase objects and mathematically assigned to the phase sample.

$u_R(\boldsymbol{r}_R)T_R(\boldsymbol{r}_R)H(\boldsymbol{r}', \boldsymbol{r}_R)$. The resulting light fields from the observed and reference samples, $U_S(\boldsymbol{r}')$ and $U_R(\boldsymbol{r}')$, are directed to the same image plane, where a CCD is placed [Fig. 1(a)]. Light fields originating from points $\boldsymbol{r}_S$ and $\boldsymbol{r}_R$ interfere in the image plane depending on their correlation given by $\Gamma(\boldsymbol{r}_S - \boldsymbol{r}_R)$ and create a hologram acquired by the CCD. The intensity of the hologram is obtained by averaging because the complex sample images stem from randomly oscillating illumination, $I_H(\boldsymbol{r}') = \left\langle \left| U_S(\boldsymbol{r}') + U_R(\boldsymbol{r}') \right|^2 \right\rangle$. In QPI, the phase is restored from the cross term $\gamma(\boldsymbol{r}') = \left\langle U_S(\boldsymbol{r}') U_R^*(\boldsymbol{r}') \right\rangle$, separated from the hologram using the spatial or temporal phase shifting.[17] In the experiment, the reference sample introduces a homogeneous phase shift $\varphi_R = \arg(T_R)$ into transmitted light. The phase obtained by the hologram processing is given by

$$\phi(\boldsymbol{r}') = \arg\{\gamma(\boldsymbol{r}')\} = \varphi_S(\boldsymbol{r}') - \varphi_R. \tag{1}$$

In $\phi(\boldsymbol{r}')$, the spatially varying phase $\varphi_S(\boldsymbol{r}')$, restoring the sample phase, is compared to a constant reference phase φ_R. In this study, $\phi(\boldsymbol{r}')$ given by (1) is referred to as the phase image. Disregarding light diffraction, point-to-point imaging by microscopes in interferometric paths is possible. Hence, only the light from one point of the observed sample contributes to the related image point $\boldsymbol{r}'$. This results in a perfect reconstruction of the sample phase, $\phi(\boldsymbol{r}') = \arg\{T_S(\boldsymbol{r}'/m)\} - \varphi_R$, where m is a microscope lateral magnification. In experiments, the image of a point object spreads to a diffraction spot. The phase change of light introduced at different sample points $\boldsymbol{r}_S$ is then transferred to the same point $\boldsymbol{r}'$ of the image plane. This diffraction non-locality deteriorates the phase imaging and imposes limitations on its performance, investigated here for the first time.

The computational model is presented in Appendix, including cases with disregarded diffraction and coherent and incoherent QPI. Thanks to its flexibility, the model simply adapts to imaging objects affecting the geometric phase of light (e.g., liquid crystal molecules or metasurface nanoantennas) and preserves validity for common-path systems based on the self-reference principle (Sec. S II of the supplementary material).

B. Sample model connecting phase objects with their binary amplitude replicas

To thoroughly explore the diffraction QPI limits, the sample transmission function $T_S(\boldsymbol{r}_S)$ must be related to a particular sample model well matched to experiments. Its design is based on the idea of a sample with biological cells, but similar inspiration can be found in material sciences. The model considers a sample consisting of J microscopic objects embedded in a homogeneous, nearly transparent environment. This environment, called sample background, is determined by the amplitude transmittance t_B and the constant optical thickness l_B, which introduces the phase shift $\varphi_B = 2\pi l_B/\lambda$ in the passing light of the wavelength λ. The objects forming the sample can be of arbitrary geometric shapes determined by areas S_j. The sample model assumes that these objects are thin and sufficiently separated to prevent their overlapping. As the objects are weakly absorbing and their transmittances t_j approach t_B, they differ from the sample background only by optical paths l_j, which introduce phase shifts of light φ_j. The values of t_j and φ_j are assumed to remain constant within the areas S_j, which is well justified for microscopic objects [Fig. 1(b)]. To express the sample transmission mathematically, functions G_j are introduced, determining the position and the geometric shape of individual objects. The function G_j takes a unit value in the area S_j with the center position $\boldsymbol{r}_{S_j} = (x_{S_j}, y_{S_j})$ and a zero value outside this area [Fig. 1(b)],

$$G_j(\boldsymbol{r}_S; \boldsymbol{r}_{S_j}) = \begin{cases} 1 \text{ for } \boldsymbol{r}_S - \boldsymbol{r}_{S_j} \in S_j, \\ 0 \text{ for } \boldsymbol{r}_S - \boldsymbol{r}_{S_j} \notin S_j. \end{cases} \tag{2}$$

Hence, G_j can be considered as binary amplitude replicas of phase objects that are assigned mathematically to them. They will be referred to as assigned amplitude objects in this study. This assignment is optically significant because it intrinsically links the phase and amplitude images. It is important to note that the binary amplitude objects are not intended to alter the light's amplitude but to delineate areas where phase objects differ in optical thickness from the surrounding environment. The complex transmission

function $T_O(\boldsymbol{r}_S)$ of the entire set of phase objects is expressed using (2) as

$$T_O(\boldsymbol{r}_S) = \sum_{j=1}^{J} G_j(\boldsymbol{r}_S;\boldsymbol{r}_{S_j}) t_j e^{i\varphi_j}. \tag{3}$$

Light not hitting the phase objects is affected by the complex transmission function of the sample background $T_B(\boldsymbol{r}_S)$,

$$T_B(\boldsymbol{r}_S) = \left[1 - \sum_{j=1}^{J} G_j(\boldsymbol{r}_S;\boldsymbol{r}_{S_j})\right] t_B e^{i\varphi_B}. \tag{4}$$

In the QPI with an independent reference phase according to Fig. 1(a), both the light scattered by objects and the background light pass through the sample path. The transmission function of the observed sample is then given as $T_S(\boldsymbol{r}_S) = T_O(\boldsymbol{r}_S) + T_B(\boldsymbol{r}_S)$.

C. Interconnection of phase and correlation images in partially coherent QPI

In partially coherent QPI with two separated interferometric paths [Fig. 1(a)], light affected by a sample S with the complex transmission function $T_S(\boldsymbol{r}_S)$ is correlated with light passing through a reference sample RS with the constant transmittance t_R and phase φ_R, $T_R = t_R e^{i\varphi_R}$. Since the optical paths of the sample and reference arms are balanced in the QPI experiments, it is justified to consider that $\varphi_R = \varphi_B$. As shown in Appendix, the phase image (1) can then be written as

$$\phi(\boldsymbol{r}') = \arg\left\{\sum_{j=1}^{J} P_j(\boldsymbol{r}')\left[t_j e^{i(\varphi_j-\varphi_B)} - t_B\right] + t_B P\right\}, \tag{5}$$

where

$$P_j(\boldsymbol{r}') = \iint_{-\infty}^{\infty} G_j(\boldsymbol{r}_S;\boldsymbol{r}_{S_j}) \Gamma(\boldsymbol{r}_S - \boldsymbol{r}_R) H(\boldsymbol{r}',\boldsymbol{r}_S) H^*(\boldsymbol{r}',\boldsymbol{r}_R) d^2 r_S d^2 r_R, \tag{6}$$

$$P = \iint_{-\infty}^{\infty} \Gamma(\boldsymbol{r}_S - \boldsymbol{r}_R) H(\boldsymbol{r}',\boldsymbol{r}_S) H^*(\boldsymbol{r}',\boldsymbol{r}_R) d^2 r_S d^2 r_R. \tag{7}$$

The phase image (5) is affected by the transmittances t_j and t_B of the sample objects and background. The terms with objects' phases $e^{i(\varphi_j-\varphi_B)}$ are superimposed with the spatially varying weights $P_j(\boldsymbol{r}')$. They represent the images of the assigned amplitude objects G_j given by (2), depending on the light correlation $\Gamma(\boldsymbol{r}_S - \boldsymbol{r}_R)$ between sample and reference sample points and the complex impulse responses $H(\boldsymbol{r}',\boldsymbol{r}_S)$ and $H(\boldsymbol{r}',\boldsymbol{r}_R)$ of identical microscopes in the sample and reference paths. P does not change at the image positions $\boldsymbol{r}'$ and represents the normalization factor. The discovered relation (5) is essential for phase imaging theory as (i) supports general insight into the formation of phase images, (ii) reveals the intrinsic interconnection between phase and amplitude images in QPI with partially coherent light, and (iii) allows assessment of optical performances and estimation of their diffraction limits in coherent and incoherent QPI.

D. Interconnection of phase and intensity images in incoherent (self-correlation) QPI

In the case of incoherent light with $\Gamma(\boldsymbol{r}_S - \boldsymbol{r}_R) \propto \delta(\boldsymbol{r}_S - \boldsymbol{r}_R)$ (Appendix), the restored phase image preserves the form (5), and the integrals determining P_j and P simplify to

$$P_j(\boldsymbol{r}') = \int_{-\infty}^{\infty} G_j(\boldsymbol{r}_S;\boldsymbol{r}_{S_j}) h^2(\boldsymbol{r}' - m\boldsymbol{r}_S) d^2 r_S, \tag{8}$$

$$P = \int_{-\infty}^{\infty} h^2(\boldsymbol{r}' - m\boldsymbol{r}_S) d^2 r_S, \tag{9}$$

where h and m denote the amplitude impulse response function given in Appendix and lateral magnification of microscopes in the sample and reference paths. $P_j(\boldsymbol{r}')$ is now determined as the convolution of G_j and microscope Point Spread Function (PSF) h^2 and represents the intensity image of the assigned amplitude object G_j. The normalization factor P indicates the total optical power of the PSF. Assuming that the differences between the objects' phases and the background phase are small, $\varphi_j - \varphi_B \ll \pi$, the reconstructed phase image (5) can be simplified to

$$\phi(\boldsymbol{r}') = \frac{\sum_{j=1}^{J} F_j(\boldsymbol{r}') t_j (\varphi_j - \varphi_B)}{\sum_{j=1}^{J} F_j(\boldsymbol{r}')(t_j - t_B) + t_B}, \tag{10}$$

where $F_j(\boldsymbol{r}') = P_j(\boldsymbol{r}')/P$ are the normalized intensity images of the assigned amplitude objects G_j taking values $0 \le F_j \le 1$. This result simply shows how the phase image arises in the incoherent QPI and is well-suited for assessing images of phase targets and biological cells used in the presented experiments. Differences between the exact and approximate descriptions of the phase images (5) and (10) are discussed in Sec. S I of the supplementary material, particularly for higher phase strokes of the imaged objects.

III. RESULTS OF NUMERICAL SIMULATIONS

A. Incoherent single-object phase imaging

As a particular case of (5)–(10), we examine the phase imaging of a single phase object with a geometric shape S_1 and its center at $\boldsymbol{r}_{S_1}$, unaffected by any other objects. For the moment, we assume that the object and background transmittances are the same, $t_1 = t_B$. Using (10) with $J = 1$, the phase restored at the image plane simplifies to

$$\phi(\boldsymbol{r}') = F_1(\boldsymbol{r}')\varphi_{G_1}, \tag{11}$$

where $\varphi_{G_1} = \varphi_1 - \varphi_B$ is the ground-truth object phase relative to the background phase, and the spatially varying weight $F_1 = P_1/P$ is given as the normalized intensity image of the assigned amplitude object G_1. As (11) shows, the phase of the object is affected by the diffraction in the image. The reconstructed phase ϕ does not keep the constant value φ_{G_1} in the region S_1, but changes according to F_1. At the boundary of the S_1 area, the object phase φ_1 abruptly falls to the background phase φ_B. In the phase image, however, the boundary of the object area is blurred, with ϕ exhibiting only a gradual change. The steepness of this change depends on the size of the phase object, which affects the spatial change in F_1. Compared to the phase object, the image deteriorates because the object phase

$\varphi_{_1}$ is coupled with the background phase $\varphi_{_B}$. This interconnection is more apparent when the restored sample phase $\varphi_{_S} = \phi + \varphi_{_B}$ is expressed in terms of F_1, $\varphi_{_S} = F_1\varphi_1 + (1 - F_1)\varphi_{_B}$. The influence of $\varphi_{_B}$ causes the phase to be restored at the paraxial image of the object center $\boldsymbol{r}' = \boldsymbol{r}'_{S_1} = m\boldsymbol{r}_{S_1}$ to deviate from the ground-truth value φ_{G_1}. This deviation can be accepted as a measure of phase accuracy. Its estimation is performed using the percent phase error, which is defined by $\delta_{\varphi_1} = (\Delta_{\varphi_1}/\varphi_{G_1})100$, where $\Delta_{\varphi_1} = \phi(\boldsymbol{r}'_{S_1}) - \varphi_{G_1}$. The percent phase error is negative or zero in the incoherent QPI and can be written as

$$\delta_{\varphi_1} = \left[F_1(\boldsymbol{r}'_{S_1}) - 1\right]100. \tag{12}$$

The phase error (12) obtained in the low-phase approximation is independent of the phase shift φ_{G_1} introduced by the imaged object. When evaluating the phase error using the exact description of the phase image (5), δ_{φ_1} remains independent of φ_{G_1} only for such objects whose shape and size result in $F_1(\boldsymbol{r}'_{S_1}) = 0.5$. In this case, $\delta_{\varphi_1} = 50\%$ for any value of φ_{G_1}. For objects with $F_1(\boldsymbol{r}'_{S_1}) > 0.5$, the phase error decreases as φ_{G_1} increases. Conversely, for $F_1(\boldsymbol{r}'_{S_1}) < 0.5$, the error increases with increasing φ_{G_1}. The dependence of the phase error on φ_{G_1} is explained theoretically and demonstrated experimentally in Sec. S I of the supplementary material.

In Fig. 2, we demonstrate deteriorations caused by light diffraction in the phase imaging of square and rectangular objects with the same ground-truth phase $\varphi_{G_1} = 1.9$ rad. This value relates to the ground-truth phase provided by the quantitative phase target used in experiments. The phase map and phase profile along the red dashed line in Fig. 2(a) were obtained for a square object with $t_1 = t_B = 1$ (the black dashed line shows the object's phase profile). The object size $2a$ was equal to the Airy disk radius r_0 in the object space, $2a = r_0$, given by the numerical aperture of the microscope objective as $r_0 = 0.61\lambda/NA$. The phase map and red solid line phase profile were calculated using (5), (8), and (9), while the red dashed line profile resulted from the approximate relation (10). Although the observed object was not influenced by any other objects, the phase accuracy of its imaging dropped down to $\delta_{\varphi_1} = -26.2\%$. The loss of phase accuracy has an illustrative graphical interpretation. According to (11), the intensity image reduces the ground-truth phase, which takes on the value $F_1(\boldsymbol{r}'_{S_1}) = P_1(\boldsymbol{r}'_{S_1})/P$ at the image center $\boldsymbol{r}'_{S_1}$. The numerator P_1 given by (8) represents the optical power of the PSF centered at $\boldsymbol{r}'_{S_1}$, which is captured in the area $S'_1 = m^2S_1$ created as the paraxial image of the object area S_1 [Fig. 2(d)]. The denominator P determines the total optical power of the PSF. When the object is much larger than the object space Airy disk, $a \gg r_0$, almost all PSF power is captured in S'_1. Hence, $F_1(\boldsymbol{r}'_{S_1}) \cong 1$ and the image is restored with the high phase accuracy, $\delta_{\varphi_1} \cong 0$. The phase accuracy also depends on the object's shape if its size is close to r_0. This is well documented by the phase imaging of the rectangular object in Fig. 2(b). Although the width remained the same as for the square object, $2a = r_0$, the phase accuracy improved to $\delta_{\varphi_1} = -15.2\%$. This improvement comes from the higher PSF power captured in the rectangular object area with the length $2L = 4r_0$. The phase of the restored image relates to the captured PSF optical power at any point

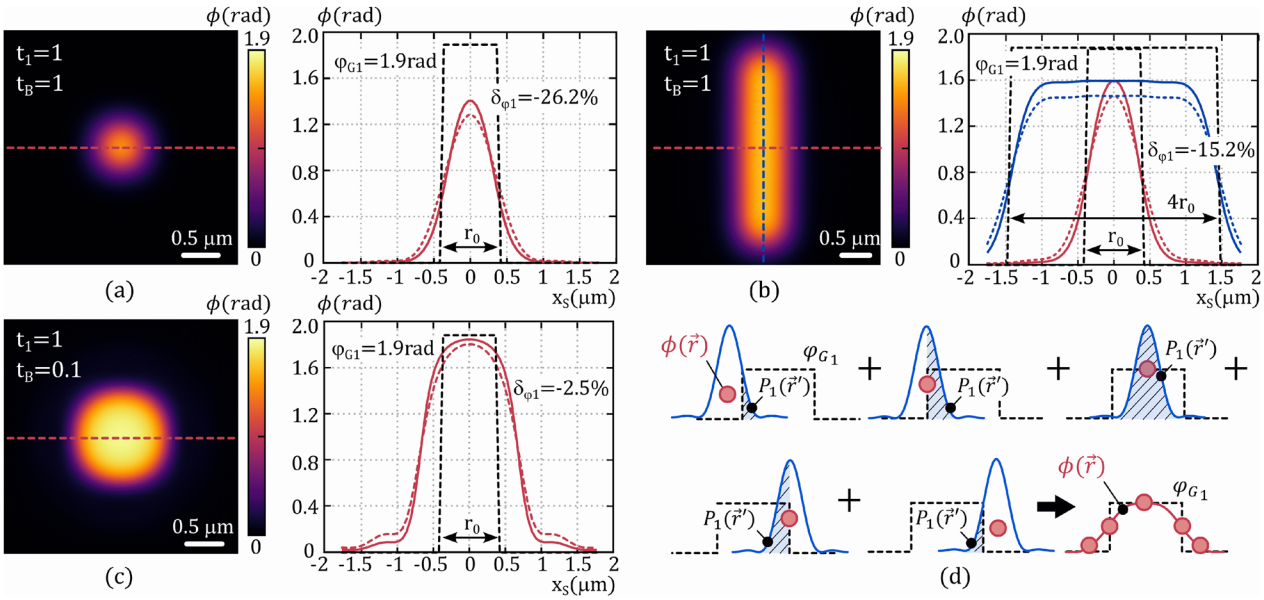

FIG. 2. Simulated phase imaging of single square and rectangular objects with the same ground-truth phase $\varphi_{G_1} = 1.9$ rad (black dashed line). Phase maps and solid line profiles were obtained by (5), (8), and (9); and dashed line profiles resulted from the low phase approximation (10). (a) Phase imaging of a transparent square object with $t_1 = t_B = 1$ and the size of $2a = r_0$ impaired by the phase error $\delta_{\varphi_1} = -26.2\%$. (b) Phase imaging of a transparent rectangular object with $t_1 = t_B = 1$, width $2a = r_0$, and length $2L = 4r_0$, providing improved phase error $\delta_{\varphi_1} = -15.2\%$. (c) Phase imaging of the same square object as in (a) but with attenuated background light, $t_1 = 1$, $t_B = 0.1$, increasing the phase accuracy to $\delta_{\varphi_1} = -2.5\%$. (d) Graphical illustration of creating the phase image $\phi = F_1\varphi_{G_1}$ (red line), where $F_1 = P_1/P$. At the image point $\boldsymbol{r}'$, the phase is proportional to the ratio of the optical power P_1 of the PSF captured in the region S'_1 to its total power P. The optical power P_1 is proportional to hatched areas illustrated for five different positions $\boldsymbol{r}'$ at the phase image ϕ, indicated by the red circles.

$\boldsymbol{r}'$ of the image plane. Five differently positioned PSFs with their centers at the object boundary and outside the object area illustrate the captured optical power P_1 [Fig. 2(d)], which explains variations in the phase image ϕ across the image plane.

The shape of the phase image is further influenced by the transmittances t_1 and t_B. When they differ, the phase error δ_{φ_1} is given by

$$\delta_{\varphi_1} = \left[F_1 - 1 + \frac{F_1(t_{1,B}-1)(1-F_1)}{F_1(t_{1,B}-1)+1}\right]100, \tag{13}$$

where $t_{1,B} = t_1/t_B$ and $F_1 \equiv F_1(\boldsymbol{r}'_{S_1})$. The $F_1 - 1$ term is always negative in incoherent QPI experiments and corresponds to δ_{φ_1} given by (12) for $t_{1,B} = 1$. When the light from the sample background is attenuated $(t_{1,B} > 1)$, the fraction in (13) becomes positive, reducing the error's magnitude. This is shown in Fig. 2(c), obtained for a square object with $2a = r_0$ and $t_{1,B} = 10$. By weakening the influence of the background phase φ_B, the reconstruction of the object phase φ_{G_1} in its center is less affected. Thanks to this, the phase image of the same object, as shown in Fig. 2(a), is restored accurately with $\delta_{\varphi_1} = -2.5\%$. However, this effect is unfavorable at the object boundary. The dominance of φ_{G_1} is extended even into the near sample background area, which causes the undesirable spatial spreading of the phase image.

Perfect phase imaging should faithfully restore the constant phase $\phi = \varphi_{G_1}$ in the object area and zero phase $\phi = 0$ outside this area. As (11) shows, this is possible only when $F_1(\boldsymbol{r}') = 1$ for $\boldsymbol{r}' \in S'_1$ and $F_1(\boldsymbol{r}') = 0$ for $\boldsymbol{r}' \notin S'_1$. These conditions correspond to an ideal point imaging with the PSF given by the Dirac delta function. This agrees with Appendix, examining the perfect QPI disregarding light diffraction.

B. Incoherent two-object phase imaging

To assess how the phase objects influence each other, the phase image (10) was examined for two objects with their centers at positions $\boldsymbol{r}_{S_1}$ and $\boldsymbol{r}_{S_2}$. The objects introduce constant phase shifts φ_1 and φ_2 in the areas S_1 and S_2, and the change in the light phase coming from the sample background is φ_B. If we assume that the objects and background are fully transparent, $t_1 = t_2 = 1$, $t_B = 1$, the restored phase image can be written as

$$\phi(\boldsymbol{r}') = F_1(\boldsymbol{r}')\varphi_{G_1} + F_2(\boldsymbol{r}')\varphi_{G_2}. \tag{14}$$

The phase image is determined by the superposition of objects' phases referenced to the background phase, $\varphi_{G_j} = \varphi_j - \varphi_B$, $j = 1, 2$. The constant phases φ_{G_j} get spatially varying support from the weighting functions $F_j(\boldsymbol{r}') = P_j(\boldsymbol{r}')/P$, which represent the normalized intensity images of the assigned amplitude objects G_j. When restoring the phase at the paraxial image of the first object's center $\boldsymbol{r}'_{S_1}$, the PSF centered at this point determines the factor $F_1(\boldsymbol{r}'_{S_1})$ supporting the phase φ_{G_1}. Its value is proportional to the PSF optical

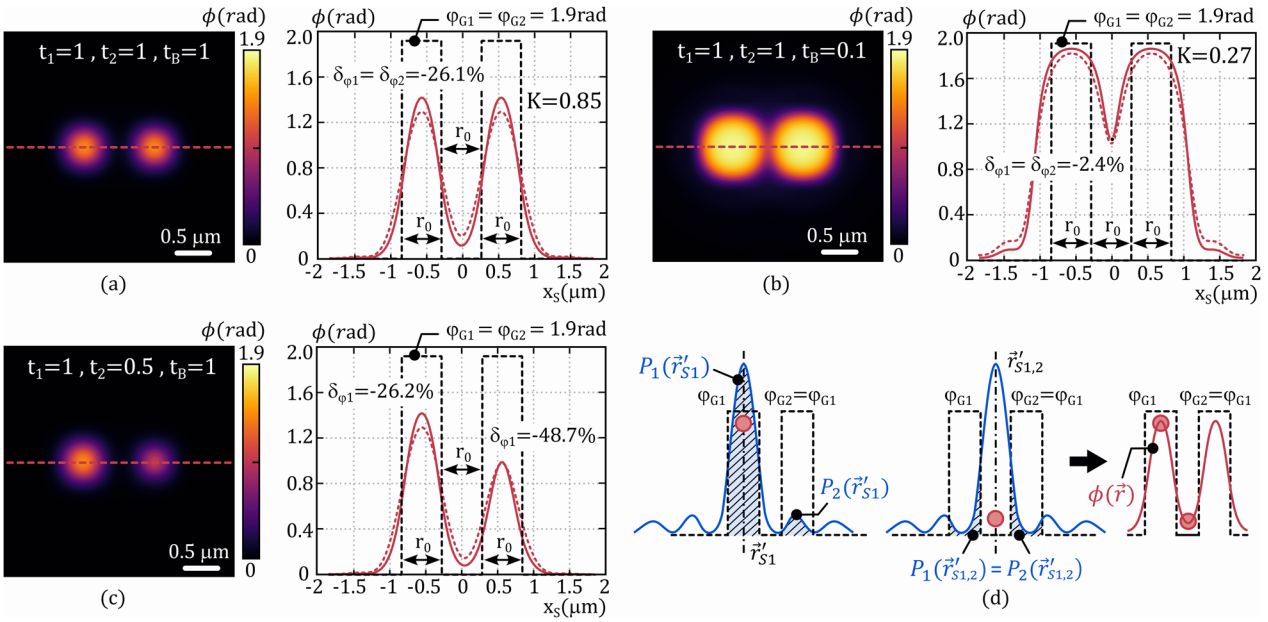

FIG. 3. Simulated phase imaging of two square objects with the same size $2a_1 = 2a_2 = r_0$ and ground-truth phase $\varphi_{G_1} = \varphi_{G_2} = 1.9$ rad. Phase maps and solid line profiles were obtained by (5), (8), and (9); and dashed line profiles resulted from the low-phase approximation (10). (a) Phase image for full transparency of objects and sample background, $t_1 = t_2 = t_B = 1$. (b) Phase image with improved phase accuracy achieved by attenuating the background light ($t_1 = t_2 = 1$, $t_B = 0.1$). (c) Phase image demonstrating degradation of phase accuracy caused by reduced transmittance of one of the objects ($t_1 = 1$, $t_2 = 0.5$, $t_B = 1$). (d) Graphical illustration of creating the two-object phase image $\phi = \left[P_1\varphi_{G_1} + P_2\varphi_{G_2}\right]/P$, where P is the total PSF optical power. The weights P_1 and P_2, which determine the image phase at the points $\boldsymbol{r}'_{S_1}$ and $\boldsymbol{r}'_{S_{1,2}}$ (red circles), are proportional to the hatched areas of the PSFs centered at $\boldsymbol{r}'_{S_1}$ and $\boldsymbol{r}'_{S_{1,2}}$, respectively. From the phase values at the object center and in the middle between the objects, the phase visibility K is determined according to (16).

power $P_1(\boldsymbol{r}'_{S_1})$ captured in the area S'_1 formed as the paraxial image of the object area S_1. The weighting factor $F_2(\boldsymbol{r}'_{S_1})$ determines how the phase of the second object φ_{G_2} affects the reconstruction of phase $\phi(\boldsymbol{r}'_{S_1})$. The value of this factor is determined by the optical power of the PSF centered at $\boldsymbol{r}'_{S_1}$, which is captured in the S'_2 area, $P_2(\boldsymbol{r}'_{S_1})$, as shown in Fig. 3(d). The phase error δ_{φ_1} indicating the reconstruction accuracy of phase $\phi(\boldsymbol{r}'_{S_1})$ at the point $\boldsymbol{r}'_{S_1}$ is given by

$$\delta_{\varphi_1} = \left[F_1(\boldsymbol{r}'_{S_1}) - 1 + F_2(\boldsymbol{r}'_{S_1})\frac{\varphi_{G_2}}{\varphi_{G_1}}\right]100. \tag{15}$$

The factor $F_2(\boldsymbol{r}'_{S_1})$ strongly depends on the distance between objects and is negligible when their images are well resolved. The phase accuracy is then the same as that of a single object (12). Figure 3(a) well documents this case. Two identical square objects with sizes $2a_1 = 2a_2 = r_0$, ground-truth phases $\varphi_{G_1} = \varphi_{G_2} = 1.9$ rad, and transmittances $t_1 = t_2 = t_B = 1$ are restored there with the same phase accuracy $\delta_{\varphi_1} = \delta_{\varphi_2} = -26.1\%$ as the single object in Fig. 2(a) with the same parameters. This shows that the phase accuracy was not affected by the second object of the sample when the objects' centers were $2r_0$ apart.

We quantify the spatial phase resolution using the phase visibility, which is introduced for two objects with identical geometric shapes $S_1 \equiv S_2$, equal ground-truth phases $\varphi_{G_1} = \varphi_{G_2}$, and centers at positions $\boldsymbol{r}_{S_1}$ and $\boldsymbol{r}_{S_2}$ (paraxial images of the objects' centers are $\boldsymbol{r}'_{S_1} = m\boldsymbol{r}_{S_1}$ and $\boldsymbol{r}'_{S_2} = m\boldsymbol{r}_{S_2}$). The phase visibility is defined by $K = |\phi_1 - \phi_{1,2}|/|\phi_1 + \phi_{1,2}|$, where $\phi_1 \equiv \phi_1(\boldsymbol{r}'_{S_1})$ and $\phi_{1,2} \equiv \phi_{1,2}(\boldsymbol{r}'_{S_{1,2}})$ are the image phases (10) restored at $\boldsymbol{r}'_{S_1}$ and $\boldsymbol{r}'_{S_{1,2}} = (\boldsymbol{r}'_{S_1} + \boldsymbol{r}'_{S_2})/2$, respectively. Using (10) and assuming that the sample objects and background do not absorb light, $t_1 = t_2 = t_B = 1$, the phase visibility can be written as

$$K = \frac{F^{(-)}}{F^{(+)}}, \quad F^{(\mp)} = F_1(\boldsymbol{r}'_{S_1}) + F_2(\boldsymbol{r}'_{S_1}) \mp 2F_1(\boldsymbol{r}'_{S_{1,2}}). \tag{16}$$

To achieve acceptable phase imaging accuracy, the size of the sample objects rescaled to image space must be larger than the Airy spot. $F_2(\boldsymbol{r}'_{S_1})$ can then be neglected in (16), as evident from Fig. 3(d). When the objects are far enough apart, their images are well resolved with $K \cong 1$, as $F_1(\boldsymbol{r}'_{S_1}) \gg 2F_1(\boldsymbol{r}'_{S_{12}})$. As the objects approach, the phase visibility decreases and completely vanishes ($K = 0$) in close objects' contact when $F_1(\boldsymbol{r}'_{S_1}) = 2F_1(\boldsymbol{r}'_{S_{12}})$ [Fig. 3(d)]. Square objects of equal size $2a_1 = 2a_2 = r_0$ with centers $2r_0$ apart are imaged with the high phase visibility $K = 0.85$, as Fig. 3(a) shows. The influence of background light attenuation ($t_B = 0.1$) on the phase image is shown in Fig. 3(b), which illustrates the results obtained using (5), (8), and (9). Compared to the image of the same objects in Fig. 3(a), phase accuracy was improved more than tenfold ($\delta_{\varphi_1} = \delta_{\varphi_2} = -2.4\%$) at the cost of contrast decreasing ($K = 0.27$). This occurs because the dominance of objects' phases φ_1 and $\varphi_2 = \varphi_1$ over φ_B is strengthened not only in the areas S_1 and S_2 but also outside of them in the sample background area. On the contrary, if the phase weight of the second object was weakened by reducing the transmittance to $t_2 = 0.5$, its image was reconstructed with degraded phase accuracy ($\delta_{\varphi_2} = -48.7\%$) compared to the transparent object with $t_1 = 1$, whose phase error remained unchanged ($\delta_{\varphi_1} = -26.2\%$) [Fig. 3(c)].

IV. EXPERIMENTAL RESULTS

A. Experiments with quantitative phase targets

In experiments, we focused primarily on exploring the limits of phase accuracy and spatial phase resolution in incoherent QPI and comparing them with the developed theory. Using extensive numerical calculations, the effects of partial light coherence and optical aberrations were also investigated. Measurements were conducted using the coherence-controlled holographic microscope in Fig. 1(a), commercially available as Telight Q-Phase. To create phase images approaching the diffraction limits, external effects and disturbances reducing the measurement precision were effectively suppressed during the experiments. This was achieved by using thermal enclosures, vibration isolation, and software-controlled autofocus. With these measures, a phase precision of 0.01 rad was ensured, as specified by the manufacturer. Phase measurements were performed with the quantitative phase target (Benchmark Technologies) with seven distinct nominal feature heights varied from 50 to 350 nm (step of 50 nm). The phase target used in the experiments was certified as fully transparent and is composed of an acrylate polymer on Corning Eagle XG glass. Due to the very low absorption of both materials, the target exhibits uniform transmittance. The presented measurements were performed with four target elements with geometrical heights of 58.6, 172.5, 272, and 383.7 nm. These refined values were obtained by the atomic force microscopy (AFM) measurement in the area of 250×250 μm^2 and were taken from the manufacturer's protocol. For the light wavelength $\lambda = 660$ nm and the refractive index of the target material $n = 1.52$, the geometrical heights determine the phase shifts of 0.29, 0.85, 1.35, and 1.9 rad. The images of groups 6 and 7 of the quantitative phase target are shown in Figs. 4(a)–4(d) for these four ground-truth phase shifts. The images were reconstructed from incoherent off-axis holograms recorded with illumination and imaging numerical apertures of 0.52 and 0.3, respectively. Figures 4(e) and 4(f) show the phase profiles along the dashed lines marked in the square elements in Figs. 4(a)–4(d). The squares of size $2a = 35$ μm are much larger than the Airy disk in the object space, $a/r_0 = 13$. In this case, the square object area captures most of the optical power of the PSF located at its center; hence, high phase accuracy is achieved according to theory. In numerical simulations performed using (5), (8), and (9), the relative phase error δ_φ ranges from −0.5% to −1% for four evaluated phase shifts [Fig. 4(e)]. In experiments, the phase error was determined by averaging the measured phase over the square area and using the related ground-truth phase. The phase profile of the image obtained experimentally [Fig. 4(f)] agrees with that calculated, and the phase error is better than −5% for all four phase shifts.

The discovered diffraction limitations of phase accuracy and spatial phase resolution were demonstrated by imaging individual elements of groups 8 and 9, introducing the ground-truth phase shift of $\varphi_G = 1.9$ rad [Figs. 5(a) and 5(b)]. Phase profiles along the dashed lines marked in Fig. 5(b) are shown by blue full lines in Figs. 5(c) and 5(d) for group 8, elements 2–6 and group 9, elements 1–6, respectively. The ratio of the linewidth $2a$ and the object space Airy disk diameter $2r_0$ varies for individual elements. The highest ratio, $a/r_0 = 0.65$, corresponds to element 2 of group 8, while the lowest ratio, $a/r_0 = 0.2$, is obtained for element 6 of group 9. According to theory, phase accuracy is affected by coupling the phase of individual lines with the background phase, which

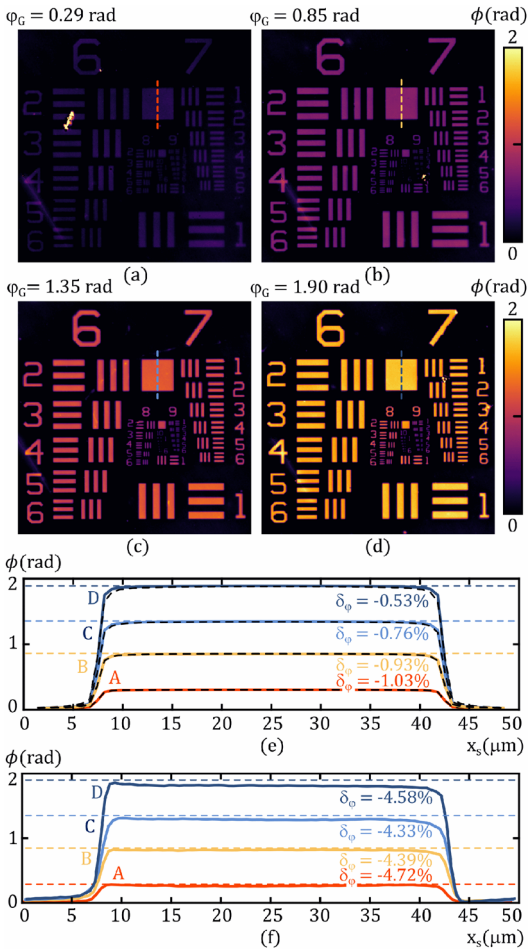

FIG. 4. (a)–(d) Incoherent quantitative phase images of groups 6 and 7 of the phase resolution target with four distinct ground-truth phase shifts φ_G = 0.29, 0.85, 1.35, and 1.9 rad. The image phase profiles of marked square objects with a/r_0 = 13 ($2a$ = 35 μm, r_0 = 1.34 μm) comparing numerical calculations (e) and experiments (f).

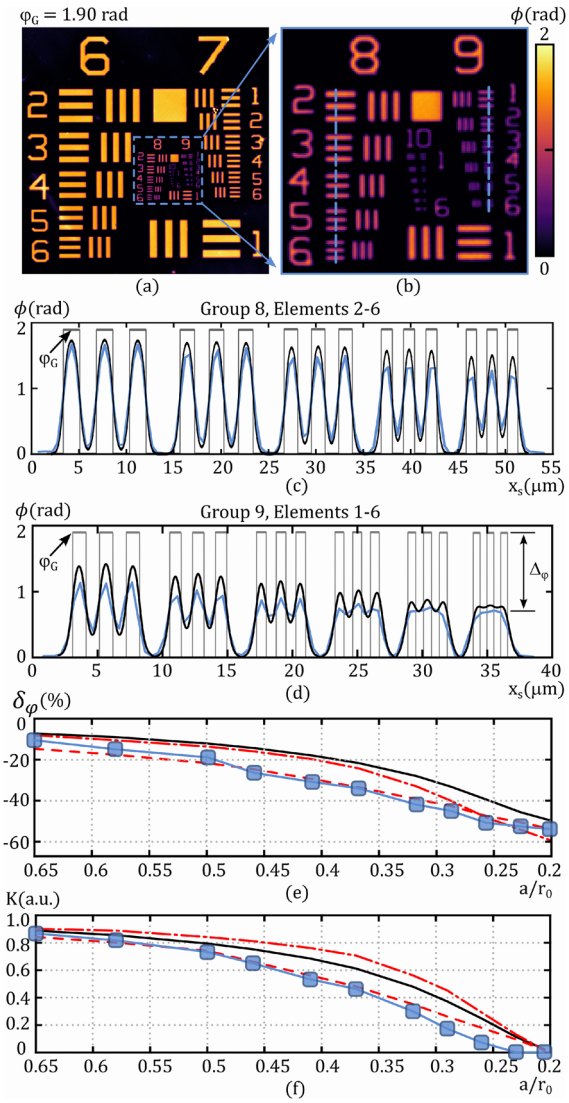

FIG. 5. Experimental phase images of (a) groups 6 and 7 and (b) groups 8 and 9 of the phase resolution target with the ground-truth phase shift φ_G = 1.9 rad. (c) and (d) Phase profiles taken along dashed lines marked in (b): experimental profiles (blue solid line), profiles obtained by calculation (5), (8), and (9) for incoherent diffraction-limited QPI (black solid line). (e) Dependence of the percent phase error δ_φ on the a/r_0 ratio: numerical calculation for incoherent diffraction-limited QPI (black solid line), experimental values assessed from the images of individual elements in (c) and (d) (blue square signs), numerical calculation for partially coherent diffraction-limited QPI (red dashed-dotted line), and numerical calculation for incoherent QPI with spherical aberration (red dashed line). (f) The same as in (e) but for the dependence of the phase visibility K on the a/r_0 ratio.

deteriorates the phase accuracy. This is evident from Figs. 5(c) and 5(d), where the deviation Δ_φ of the restored phase profiles from the ground-truth phase φ_G = 1.9 rad gradually grows with decreasing a/r_0 ratio. Both theoretical and experimental results demonstrate this trend well. In Figs. 5(c) and 5(d), the gray solid line shows the ground-truth object phase φ_G, while the blue solid line represents the phase profiles ϕ reconstructed in the experiments. The experimental data match well the simulation results provided by (5), (8), and (9) (black solid line). The deterioration of the phase error δ_φ with the decreasing a/r_0 ratio is demonstrated in Fig. 5(e). The black solid line shows the simulation results obtained for the incoherent diffraction-limited QPI, and the square signs represent δ_φ assessed from the experimental phase profiles of individual elements in Figs. 5(c) and 5(d).

From the experimental data in Fig. 5, the spatial phase resolution was also evaluated and compared with the theory of the incoherent diffraction-limited QPI. The phase visibility was determined according to (16), where the image phase at the $\mathbf{r}'_{S_1}$ point was determined by averaging three phase values taken at the centers of the lines. Similarly, the phase at $\mathbf{r}'_{S_{1,2}}$ point was obtained as the average of two phases measured between the lines. The phase visibility K degrading with the decreasing a/r_0 ratio was evaluated from

the phase images in Figs. 5(c) and 5(d) and graphically illustrated in Fig. 5(f). The black solid line represents the theory of incoherent diffraction-limited QPI, while the blue squares come from experiments. The experimental data in Figs. 5(e) and 5(f) show that phase accuracy is lost, although the lines are still well resolved. For example, element 1 from group 9 is in experiments imaged with sufficient visibility approaching $K \cong 0.5$, while the phase error increases to a hardly acceptable value of $\delta_\varphi \cong -40\%$.

As incoherent diffraction-limited QPI is experimentally unattainable, partial light coherence and optical aberrations were incorporated into the numerical simulations (Sec. S III of the supplementary material). The effect of partial coherence was analyzed for a diffraction-limited optical system with the illumination and imaging numerical apertures of 0.52 and 0.3, respectively, as used in the experiments. In this case, the spatial coherence was still low, as the coherence area was ~1.7 times smaller than the Airy disk in the sample plane. The phase error and phase visibility obtained for the partially coherent diffraction-limited QPI are shown by the red dashed-dotted lines in Figs. 5(e) and 5(f). The phase error remains almost unchanged for line tests with lower spatial frequency, but it deteriorates more significantly for the a/r_0 ratio from 0.35 to 0.2. The phase visibility is slightly improved for the a/r_0 ratio from 0.5 to 0.3. The effect of aberrations was analyzed assuming fully incoherent light. Numerical simulations were conducted for a third-order spherical aberration characterized by a coefficient of $A_{040} = \lambda/4$ (Sec. S III of the supplementary material). Although the intensity imaging maintains high quality with this aberration (a Strehl ratio of 0.8), the phase error and phase visibility are adversely affected [red dashed lines in Figs. 5(e) and 5(f)] and approach experimental values (blue square marks).

The measured data presented in Fig. 5 for $\varphi_G = 1.9$ rad were supplemented with results obtained for other ground-truth phase shifts of the target $\varphi_G = 0.29$, 0.85, and 1.35 rad. The reconstructed phase images are shown in Fig. S1 of the supplementary material. These measurements enabled us to compare the dependences of phase accuracy and visibility on the a/r_0 ratio for individual phase shifts (Fig. S2 of the supplementary material). The experimental results were further supplemented by simulations for large phase shifts, and variations in the phase error with φ_G and a/r_0 were explained theoretically (Sec. S I in the supplementary material).

A comparison of images from QPI and direct intensity imaging is performed through numerical simulations in Sec. S IV of the supplementary material for elements E1 and E6 of group G9.

The loss of phase accuracy in the image of spatially resolved structures is a critical effect that deserves attention. We further investigated it experimentally by imaging a phase Siemens star, which was previously used in the study of coherent microscopy resolution.[22] Figure 6(a) shows the entire phase image of the star, while a detail of the square area marked by the blue dashed line is illustrated in Fig. 6(b). Color-coded phase profiles taken along the semi-circles marked in the respective colors in Figs. 6(a) and 6(b) are shown in Fig. 6(c). Although the correct phase does not change radially and holds a constant value of $\varphi_G = 1.9$ rad in all sections of the star, the image phase ϕ decreases when the semi-circle radius r_S is reduced. The steep radial phase drop resulting in an unacceptable phase error is evident from the phase profile in Fig. 6(d), which was evaluated along the blue dashed line marked in Fig. 6(b). The radial drop of the image phase ϕ can be explained according to (11) and Fig. 2(d). The

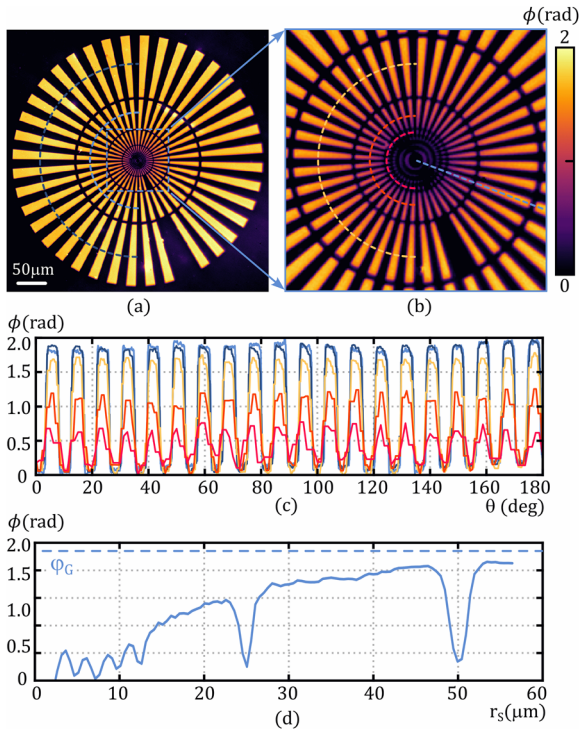

FIG. 6. Experimental phase images of a phase Siemens star with the ground-truth phase shift $\varphi_G = 1.9$ rad obtained with MO 10×, $NA = 0.3$. (a) Phase image of the entire star. (b) Phase image of the square area marked in blue dashed line in (a). (c) Color-coded phase profiles taken along semi-circles with radii $r_S = 11, 18, 37, 75$, and 150 μm, marked in (a) and (b) by respective colors. (d) Radial profile of the phase image taken along the blue dashed line marked in (b).

best phase accuracy is achieved along the outer semi-circle marked in dark blue, whose radius is $r_S = 150$ μm. On this semi-circle, the star sector is the widest and receives most of the optical power of the PSF located on its symmetry axis. The phase weight F_1 in (11) thus acquires the largest value in this position. The image phase $\phi = 1.85$ rad is reconstructed with a phase error $\delta_\varphi = -2.6\%$. On the inner semi-circle with $r_S = 11$ μm, where the sector is the narrowest, only a small part of the PSF optical power is captured by it. The low factor F_1 in (11) significantly reduces the ground-truth phase, which leads to an incorrect image phase of $\phi = 0.65$ rad related to a phase error of $\delta_\varphi = -65.7\%$. Although the star sectors are well resolved, the capability of phase quantification is lost, and the imaging provides only the phase contrast when using $NA = 0.3$ microscope objectives.

B. Experiments with biological cells

Diffraction phase accuracy deterioration demonstrated by quantitative phase target experiments was also investigated under application-appealing conditions. In experiments using a specimen with spontaneously transformed rat embryonic fibroblast (LW3K12) cells, we measured the same field of view with two different microscope objectives, namely, MO 10×, $NA = 0.3$, and 20×, $NA = 0.55$. For comparative measurements, we chose three various cells and

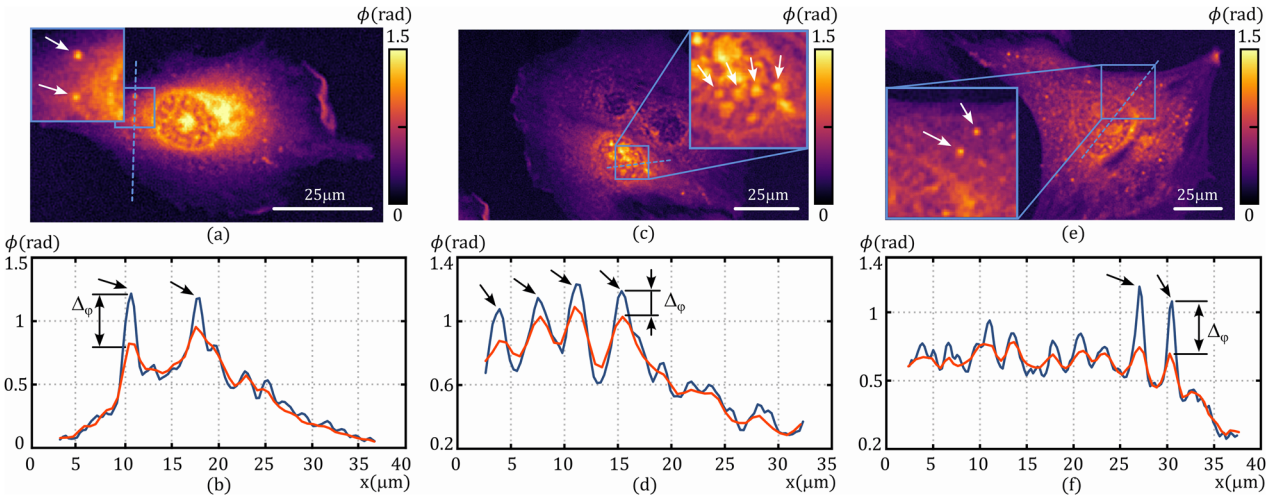

FIG. 7. Experimental phase images of spontaneously transformed rat embryonic fibroblast (LW3K12) cells. (a) Phase image of the cell with inset showing cytoplasmic vesicles. (b) Phase profiles along the dashed line in (a) measured with MO 20×, *NA* = 0.55 (blue) and MO 10×, *NA* = 0.3 (red). (c) Phase image of the cell with inset showing phase structure of the nucleus. (d) Phase profiles along the dashed line in (c) measured with *NA* = 0.55 (blue) and *NA* = 0.3 (red). (e) Phase image of the cell with inset showing components of the nucleus and cytoplasmic vesicles. (f) Phase profiles along the dashed line in (e) measured with *NA* = 0.55 (blue) and *NA* = 0.3 (red).

evaluated cross-sectional phase profiles in their different regions. The phase images of the cells in Figs. 7(a), 7(c), and 7(e) were cut out from the image captured with the MO 20×, *NA* = 0.55. The entire field of view captured by both MOs is presented in Fig. S5 of the supplementary material. For the first comparison of phase images taken by MOs with different diffraction limits, we selected the cytoplasmic vesicles in Fig. 7(a). The restored phase was evaluated along the blue dashed line intersecting vesicles marked by arrows in the enlarged inset in Fig. 7(a). The obtained phase profiles are presented in Fig. 7(b), where the blue and red lines represent the measurements performed with MOs 20×, *NA* = 0.55, and 10×, *NA* = 0.3, respectively. The profiles show that approximately the same phase values are measured in vast cytoplasmic areas with a gradual phase change. On the contrary, the phases in the centers of microscopic vesicle areas significantly differ for both measurements. When expressing the phase difference Δ_φ marked in Fig. 7(b) as a percentage of the phase value from the blue curve, a phase error of $\delta_\varphi \approx -30\%$ is obtained. This is a consequence of the diffraction effect on the phase accuracy in single-object imaging, as described by (11) and (12) and demonstrated in Fig. 2. The phase error increases as the ratio of the object and the Airy disk sizes decreases. Considering the radius of the vesicle area of ~1 μm and Airy disk radii of 1.3 and 0.7 μm for *NA* = 0.3 and *NA* = 0.55, respectively, the phase error evaluated theoretically well agrees with that obtained from measurement. The phase accuracy achieved with different numerical apertures was further assessed in the phase image of the cell nucleus in Fig. 7(c). The phase was evaluated along the blue dashed line passing through the nucleus components, marked by arrows in the enlarged inset of Fig. 7(c). The blue and red lines in Fig. 7(d) represent the phase profiles measured with MOs 20×, *NA* = 0.55, and 10×, *NA* = 0.3, respectively. The phase profiles are close to each other in the cytoplasmic cell area, but the phases differ at centers of areas in size comparable to the Airy disk. The phase difference Δ_φ from Fig. 7 corresponds to $\delta_\varphi \approx -10\%$ when expressed as previously. The difference in measurement results is reduced because the nucleus components are larger compared to cytoplasmic vesicles and the diffraction effect is less pronounced. For the last measurement in Fig. 7(e), we selected the area incorporating cytoplasm vesicles and nucleus components [inset in Fig. 7(e)]. The phase profiles along the blue dashed line are color-coded as before and presented in Fig. 7(f). Here, the significant phase errors in vesicle areas and minor errors within the nucleus structure are presented together, further supporting demonstrations in Figs. 7(b) and 7(d).

As demonstrated in Fig. 7, QPI provides a high level of detail when observing biological specimens. Consequently, QPI has become an effective tool for the quantitative study of all structures visible in the reconstructed phase images. This allowed the tracking of vesicles and organelles in living cells,[41] QPI-based Lagrangian velocimetry for intracellular net growth, mapping intracellular biomass production and degradation,[42] or digital staining of quantitative phase images.[43] These advanced QPI applications, along with many other phase-sensitive measurements, investigate structures close to the standard optical limit, where the quantitativeness of QPI is significantly compromised. Utilizing the presented QPI diffraction theory and considering its implications can ensure the correct acquisition of experimental data and avoid artifacts during processing.

V. DISCUSSION

The developed diffraction theory brings new findings affecting a wide range of holographic QPI techniques. We will briefly discuss their impact on incoherent and super-resolution QPI. The advantages of these modalities over the common-path QPI are highlighted in the supplementary material.

A. Phase error estimation in incoherent QPI

In this study, increased attention was focused on the ground-truth phase accuracy and its diffraction limitations. The phase image of a single transparent object obtained by an incoherent QPI is deteriorated by the phase error (12), which can be assessed through factor F_1. Its value is determined by the object's shape and size, the numerical aperture of the microscope objective, and the light wavelength. This way, the phase accuracy of typical observations performed with the microscope objectives used in the experiments ($NA = 0.3$ and $NA = 0.55$, $\lambda = 660$ nm) can be easily estimated. Considering an ideal optical system with a circular aperture, the PSF is given as $I_{PSF}(\rho) = [2J_1(\rho)/\rho]^2$. The optical power of the PSF encircled in the area specified by the parameter ρ_0, $P_1(\rho_0)$, and normalized by the total PSF power, P, is obtained as $F_1 = P_1(\rho_0)/P = 1 - J_0^2(\rho_0) - J_1^2(\rho_0)$. When measuring a transparent circular object with a diameter of $2a = 30$ μm (e.g., average human body cell size) by the objective with $NA = 0.3$ ($a/r_0 \cong 11$), F_1 is calculated using $\rho_0 = 2\pi aNA/\lambda = 42.8$ and gets the value $F_1 = 0.985$. The relative phase error (12) of this measurement is $\delta\varphi_1 = -1.5\%$. If the same object is imaged with $NA = 0.55$ ($a/r_0 \cong 20$), resulting in $\rho_0 = 78.5$ and $F_1 = 0.992$, high accuracy measurement determined by the relative phase error of $\delta\varphi_1 = -0.8\%$ is realized. Phase accuracy is significantly reduced in the phase images of objects with sizes closer to Rayleigh resolution. When measuring a transparent object with a size of $2a = 3$ μm (e.g., extracellular vesicles) by an objective with $NA = 0.3$ ($a/r_0 \cong 1.1$), F_1 is determined with $\rho_0 = 4.3$ and acquires a value of $F_1 = 0.84$. The relative phase error of this measurement is $\delta\varphi_1 = -16\%$. Using an objective with $NA = 0.55$ ($a/r_0 \cong 2$), giving $\rho_0 = 7.9$ and $F_1 = 0.914$, the phase error is reduced to $\delta\varphi_1 = -8.6\%$. The phase error estimation is simple and reliable, aligning well with experiments using certified phase targets and biological cells. This procedure significantly enhances QPI, as the accuracy of phase measurements determines whether the imaging is truly quantitative or merely qualitative.

B. Phase accuracy in super-resolution QPI

Techniques of synthetic apertures providing super-resolution in directly detected intensity images were also deployed in holographic microscopy.[35–38] Recently, single-shot super-resolution imaging was demonstrated by shaping a coherence gate in a holographic microscope using partially coherent light.[39] In all these implementations, the particular focus was on the transverse spatial super-resolution of phase images, demonstrated through the narrowing of the PSF below the Rayleigh limit. The theory presented here proves that the super-resolution QPI also significantly increases the phase accuracy. In the super-resolution QPI, the reference path is supplemented with amplitude or phase masks, forming a sub-diffraction impulse response.[38,39] Following this design, the PSF h^2 was replaced by the product of the amplitude responses of the sample and reference paths $h_S h_R$ when calculating the factors P_j and P by (8) and (9). For the reference path, a sub-diffraction h_R given by the zero-order Bessel function J_0 was considered,[39] whose central area is reduced compared to h_S providing the diffraction-limited spot [Eq. (A5) in Appendix]. The phase images of the resolution target reconstructed in incoherent light achieved higher phase accuracy and visibility when compared to the diffraction-limited incoherent image for all examined target groups and elements (Fig. S3 in the supplementary material). The demonstrated almost threefold increase in phase accuracy deserves particular attention. This previously unreported capability of super-resolution QPI fits well with the presented theory, and Fig. 2(d) provides an illustrative insight. The PSF h^2 located in the center of the object is replaced by the product $h_S h_R$, which forms a pattern with reduced central area and side oscillations. This leads to an increase in the optical power P_1 captured in the object area and, according to (12), to a decreased phase error. The phase accuracy enhancement can also be found in experimental super-resolution QPI obtained by the synthetic aperture method, where it remained overlooked. The color-coded phase achieves higher values for super-resolution than for a diffraction-limited image affected by a negative phase error [cf. Figs. 6(b) and 6(c) in Ďuriš *et al.*[38]].

Enhanced phase accuracy in super-resolution QPI has significant real-world implications. In biophotonics, true quantitative phase information is crucial for the measurement of dry mass, a key parameter of cells and their compartments. Similarly, in nanophotonics, the fabrication quality of plasmonic metasurfaces is assessed by analyzing the phase response of sub-diffraction nanoantennas. In both cases, inaccuracies in reconstructed quantitative data can lead to erroneous interpretations and flawed conclusions. Therefore, both high resolution and accuracy are essential, as fine sample details must be paired with accurate quantitative data to ensure reliable results.

VI. CONCLUSION

In conclusion, we developed the first comprehensive diffraction theory of QPI, revealing the diffraction limitations on imaging performance across various coherence states. An innovative phase sample modeling intrinsically connected the diffraction phase imaging theory with Rayleigh's resolution theory. This approach led to a deeper understanding of incoherent QPI and brought new ideas and stimuli throughout quantitative phase microscopy. The importance of phase accuracy was highlighted by showing that it can drop sharply, thereby compromising the quantitativeness of QPI, even when the phase image is well-resolved spatially. The role of coherence in QPI was clarified, and image restorations using either an independent reference phase or a self-reference principle were compared (Sec. S II of the supplementary material). In terms of phase accuracy, a low-coherence QPI system with an independent reference phase was proven to outperform self-reference systems that require increased spatial coherence of light. Diffraction deterioration of phase accuracy was examined theoretically and experimentally, revealing its critical sensitivity to the shape, size, and absorption of the imaged objects. The proposed phase error estimation reliably identifies experimental conditions under which the quantitative nature of imaging is compromised. This eliminates artifacts when converting the measured phase to the dry mass of cells and diagnosing phase modulation by liquid crystals and photonic metasurfaces. The discovered relationship between diffraction phase error and experimental parameters can be used to enhance phase accuracy through data post-processing or the application of machine learning. Since the QPI is closely related to optical diffraction tomography (ODT), new findings could advance this area as well. ODT employs QPI to capture 2D phase images from various illumination angles, which are subsequently used to reconstruct a

3D distribution of the sample's refractive index.[44] Therefore, previous studies that have extensively examined ODT spatial resolution[45] should be enhanced by incorporating accuracy assessments to estimate the deviations of the reconstructed refractive index from the ground truth values.

SUPPLEMENTARY MATERIAL

The supplementary material includes experimental data showing the dependence of phase accuracy and resolution on ground-truth phase stroke; simulation imaging of a phase resolution target using coherent, incoherent, and super-resolution QPI; and incoherent QPI images of biological cells supporting Fig. 7.

ACKNOWLEDGMENTS

We acknowledge the Biophotonics Core Facility, CEITEC Brno University of Technology, Czech Republic, supported by MEYS CR (LM2023050 Czech-BioImaging).

AUTHOR DECLARATIONS

Conflict of Interest

The authors have no conflicts to disclose.

Author Contributions

Zdeněk Bouchal: Conceptualization (equal); Formal analysis (equal); Methodology (equal); Software (equal); Supervision (equal); Writing – original draft (equal); Writing – review & editing (equal). **Petr Bouchal**: Data curation (equal); Formal analysis (equal); Software (equal); Visualization (equal); Writing – review & editing (equal). **Tereza Chmelíková**: Resources (lead); Software (equal). **Jaromír Fiurášek**: Supervision (equal); Writing – review & editing (equal).

DATA AVAILABILITY

The raw experimental data that support the findings of this study are openly available in Figshare at https://doi.org/10.6084/m9.figshare.26355913.v1.

APPENDIX: THEORETICAL APPROACHES

1. Calculation model of partially coherent QPI

In the holographic QPI [Fig. 1(a)], two identical microscopes with the same complex impulse response function H create images of the observed and reference samples with coordinates $\boldsymbol{r}_S = (x_S, y_S)$ and $\boldsymbol{r}_R = (x_R, y_R)$, respectively, in the same image plane $\boldsymbol{r}' = (x', y')$. The complex amplitudes of the images can be written as

$$U_j(\boldsymbol{r}') = \int_{-\infty}^{\infty} u(\boldsymbol{r}_j) T_j(\boldsymbol{r}_j) H(\boldsymbol{r}', \boldsymbol{r}_j) d^2 r_j, \quad j = S, R, \tag{A1}$$

where T_S and T_R are the complex transmission functions of the observed and reference samples, and u denotes the complex amplitude of the illumination. The impulse response is obtained by solving Fresnel diffraction integrals for a system consisting of a microscope objective (MO) and a tube lens (TL). The paraboloidal wave is emitted from points $\boldsymbol{r}_j$ of the front focal planes of identical MOs in the sample and reference paths ($j = S, R$). The MOs have a focal length of f_0 and are transversely unbounded, transforming the incident divergent wave into a plane wave. The light wave incident on the TL with focal length f_T is bound by the lens aperture determined by the pupil function P_T. In the approach used, the complex impulse response at the back focal plane of the TL can be written as

$$H(\boldsymbol{r}', \boldsymbol{r}_j) \propto e^{i\Omega(\boldsymbol{r}', \boldsymbol{r}_j)} h(\boldsymbol{r}' - m\boldsymbol{r}_j), \quad j = S, R, \tag{A2}$$

where an unimportant term was omitted and

$$\Omega(\boldsymbol{r}', \boldsymbol{r}_j) = \frac{k\left(m^2 |\boldsymbol{r}_j|^2 - |\boldsymbol{r}'|^2\right)}{2 f_T}, \tag{A3}$$

$$h(\boldsymbol{r}' - m\boldsymbol{r}_j) = \int_{-\infty}^{\infty} P_T \exp\left\{ i \frac{k}{f_T} \left[\boldsymbol{r}_T \cdot (\boldsymbol{r}' - m\boldsymbol{r}_j) \right] \right\} d^2 r_T. \tag{A4}$$

With P_T determining the circular aperture and providing the numerical aperture NA_T of the TL, the integral (A4) gives the Airy pattern,

$$h(\boldsymbol{r}' - m\boldsymbol{r}_j) = \frac{2 J_1(V_j)}{V_j}, \tag{A5}$$

where

$$V_j = k NA_T |\boldsymbol{r}' - m\boldsymbol{r}_j|.$$

In the Fresnel approximation, the isoplanatic shift appears in the amplitude of complex impulse response while is not justified in its quadratic phase. The images U_S and U_R are superimposed on a CCD, creating a holographic record. Since the illumination field u comes from a spatially incoherent source and oscillates randomly, the hologram intensity is obtained by averaging as $I_H = \langle |U_S + U_R|^2 \rangle$. The observed sample phase is stored in a cross-holographic term $\gamma = \langle U_S U_R^* \rangle$. When using the Köhler illumination, the light u entering the sample and reference object planes is given by Fourier transforming the complex amplitude A of the light leaving the source, $u = \mathcal{F}\{A\}$. The considered spatially incoherent source is delta-correlated, $\langle A(\boldsymbol{R}) A^*(\boldsymbol{R}') \rangle = I(\boldsymbol{R}) \delta(\boldsymbol{R} - \boldsymbol{R}')$, meaning the light from different source points is completely uncorrelated and has intensity I at a source point $\boldsymbol{R} = (X, Y)$. In this case, γ is calculated as

$$\gamma(\boldsymbol{r}') = \iint_{-\infty}^{\infty} \Gamma(\boldsymbol{r}_S - \boldsymbol{r}_R) T_S(\boldsymbol{r}_S) T_R^*(\boldsymbol{r}_R) H(\boldsymbol{r}', \boldsymbol{r}_S) H^*(\boldsymbol{r}', \boldsymbol{r}_R) d^2 r_S d^2 r_R, \tag{A6}$$

where Γ describes the light correlation between different points of the object planes in the signal and reference paths. According to the van Cittert–Zernike theorem, Γ is calculated by the Fourier transform of the source intensity I,

$$\Gamma(\boldsymbol{r}_S - \boldsymbol{r}_R) = \frac{1}{\Gamma_0} \int_{-\infty}^{\infty} I(\boldsymbol{R}) \exp\left[-i 2\pi \boldsymbol{R} \cdot (\boldsymbol{r}_S - \boldsymbol{r}_R) / \lambda f \right] d^2 R, \tag{A7}$$

where f is the focal length of the condenser lens, λ denotes the light wavelength *in vacuo*, and $\Gamma_0 = \Gamma(0)$. In QPI experiments, the reference sample is homogeneous; hence, the constant transmission

T_R^* can be placed before the integral (A6). The phase ϕ obtained from γ then provides the difference between the reconstructed sample phase φ_S and the constant reference phase $\varphi_R = \arg(T_R)$ given by (1) and referred to as the phase image. The phase image reconstruction given by (A6) and (A7) and (1) includes three specific cases with different manifestations of diffraction and coherence of light.

2. Perfect QPI disregarding light diffraction

Light diffraction inevitably accompanies all QPI experiments. Diffraction effects disappear only in the calculation model describing the interferometer optical systems by ray optics. In this approach, the optical systems provide point imaging whose amplitude impulse response becomes a Dirac delta function, $h(\boldsymbol{r}' - m\boldsymbol{r}_j) = \delta(\boldsymbol{r}' - m\boldsymbol{r}_j), j = S, R$. The phase image obtained from (A6) and (A7) and (1) is given by $\phi(\boldsymbol{r}') = \arg\{T_S(\boldsymbol{r}'/m)\} - \arg\{T_R\}$, which means that the difference between the sample and reference phases is faithfully restored irrespective of the light coherence. In the perfect QPI, the light originating from optically conjugated points of the sample and the reference object with the coordinates $\boldsymbol{r}_S$ and $\boldsymbol{r}_R$ is focused by optical systems to the same image point $\boldsymbol{r}' = m\boldsymbol{r}_S = m\boldsymbol{r}_R$. This ensures that the phase from each sample point is restored without damage at the related image point. In real QPI experiments, light transfers the phase from the single sample point to a small image area determined by the diffraction spot. Consequently, the phase reconstruction at a given sample point is affected by the phase at other nearby sample and background points. This results in a diffraction deterioration of the restored phase, depending on the light coherence.

3. Coherent QPI

The correlation of light illuminating the sample and the reference object increases as the source size decreases. In the limiting case of a point source with intensity given by $I \propto \delta(\boldsymbol{R})$, fully coherent illumination with $\Gamma = 1$ is obtained, as follows from (A7). In this case, the phase of the complex impulse response H acts unfavorably. The reconstruction of the sample phase is undesirably affected by the phase differences $\Delta\Omega = \Omega(\boldsymbol{r}', \boldsymbol{r}_S) - \Omega(\boldsymbol{r}', \boldsymbol{r}_R)$ at individual points of the sample and the reference object, which are integrated into (A6).

4. Incoherent (self-correlation) QPI

In another theoretical coherence limit, a constant intensity $I = I_0$ is assumed across an infinitely large source. In this case, Eq. (A7) results in $\Gamma \propto \delta(\boldsymbol{r}_S - \boldsymbol{r}_R)$, meaning the illumination is completely incoherent. The interference then occurs only for light emanating from points whose paraxial-ray images coincide in the image plane (so-called self-interference). When incoherently illuminating the sample and the reference object, the phase restoration (5) is performed with γ given by

$$\gamma(\boldsymbol{r}') = \int_{-\infty}^{\infty} T_S(\boldsymbol{r}_S) T_R^*(\boldsymbol{r}_S) \left|H(\boldsymbol{r}' - m\boldsymbol{r}_S)\right|^2 d^2 r_S. \tag{A8}$$

In the incoherent QPI, the phase is restored through the intensity impulse response $|H|^2 = h^2$, known as the Point Spread Function (PSF). This is an advantage over the coherent QPI, as undesirable effects of the quadratic phase and π phase jumps of the complex impulse function H are eliminated. The image is further enhanced by removing the speckle noise.

REFERENCES

[1] F. Zernike, "Phase contrast, a new method for the microscopic observation of transparent objects part II," Physica **9**(10), 974–986 (1942).
[2] H. Majeed, S. Sridharan, M. Mir, L. Ma, E. Min, W. Jung, and G. Popescu, "Quantitative phase imaging for medical diagnosis," J. Biophotonics **10**(2), 177–205 (2017).
[3] Z. Huang and L. Cao, "Quantitative phase imaging based on holography: Trends and new perspectives," Light: Sci. Appl. **13**(1), 145 (2024).
[4] Y. Park, C. Depeursinge, and G. Popescu, "Quantitative phase imaging in biomedicine," Nat. Photonics **12**(10), 578–589 (2018).
[5] M. J. Escuti, J. Kim, and M. W. Kudenov, "Controlling light with geometric-phase holograms," Opt. Photonics News **27**(2), 22–29 (2016).
[6] C. P. Jisha, S. Nolte, and A. Alberucci, "Geometric phase in optics: From wavefront manipulation to waveguiding," Laser Photonics Rev. **15**(10), 2100003 (2021).
[7] P. Chen, B. Wei, W. Hu, and Y. Lu, "Liquid-crystal-mediated geometric phase: From transmissive to broadband reflective planar optics," Adv. Mater. **32**(27), 903665 (2020).
[8] A. V. Kildishev, A. Boltasseva, and V. M. Shalaev, "Planar photonics with metasurfaces," Science **339**(6125), 1232009 (2013).
[9] N. Yu and F. Capasso, "Flat optics with designer metasurfaces," Nat. Mater. **13**(2), 139–150 (2014).
[10] L. Huang, S. Zhang, and T. Zentgraf, "Metasurface holography: From fundamentals to applications," Nanophotonics **7**(6), 1169–1190 (2018).
[11] J. Babocký, A. Křížová, L. Štrbková, L. Kejík, F. Ligmajer, M. Hrtoň, P. Dvořák, M. Týč, J. Čolláková, V. Křápek, R. Kalousek, R. Chmelík, and T. Šikola, "Quantitative 3D phase imaging of plasmonic metasurfaces," ACS Photonics **4**(6), 1389–1397 (2017).
[12] P. Bouchal, P. Dvořák, J. Babocký, Z. Bouchal, F. Ligmajer, M. Hrtoň, V. Křápek, A. Faßbender, S. Linden, R. Chmelík, and T. Šikola, "High-resolution quantitative phase imaging of plasmonic metasurfaces with sensitivity down to a single nanoantenna," Nano Lett. **19**(2), 1242–1250 (2019).
[13] P. C. Chaumet, P. Bon, G. Maire, A. Sentenac, and G. Baffou, "Quantitative phase microscopies: Accuracy comparison," Light: Sci. Appl. **13**(1), 288 (2024).
[14] P. Marquet, B. Rappaz, P. J. Magistretti, E. Cuche, Y. Emery, T. Colomb, and C. Depeursinge, "Digital holographic microscopy: A noninvasive contrast imaging technique allowing quantitative visualization of living cells with subwavelength axial accuracy," Opt. Lett. **30**(5), 468 (2005).
[15] T. Ikeda, G. Popescu, R. R. Dasari, and M. S. Feld, "Hilbert phase microscopy for investigating fast dynamics in transparent systems," Opt. Lett. **30**(10), 1165 (2005).
[16] D. O. Hogenboom, C. A. DiMarzio, T. J. Gaudette, A. J. Devaney, and S. C. Lindberg, "Three-dimensional images generated by quadrature interferometry," Opt. Lett. **23**(10), 783 (1998).
[17] I. Yamaguchi and T. Zhang, "Phase-shifting digital holography," Opt. Lett. **22**(16), 1268 (1997).
[18] G. Popescu, L. P. Deflores, J. C. Vaughan, K. Badizadegan, H. Iwai, R. R. Dasari, and M. S. Feld, "Fourier phase microscopy for investigation of biological structures and dynamics," Opt. Lett. **29**(21), 2503 (2004).
[19] C. Edwards, A. Arbabi, G. Popescu, and L. L. Goddard, "Optically monitoring and controlling nanoscale topography during semiconductor etching," Light: Sci. Appl. **1**(9), e30 (2012).
[20] Z. Wang, L. Millet, M. Mir, H. Ding, S. Unarunotai, J. Rogers, M. U. Gillette, and G. Popescu, "Spatial light interference microscopy (SLIM)," Opt. Express **19**(2), 1016 (2011).
[21] P. Bouchal, L. Štrbková, Z. Dostál, R. Chmelík, and Z. Bouchal, "Geometric-phase microscopy for quantitative phase imaging of isotropic, birefringent and space-variant polarization samples," Sci. Rep. **9**(1), 3608 (2019).

[22]R. Horstmeyer, R. Heintzmann, G. Popescu, L. Waller, and C. Yang, "Standardizing the resolution claims for coherent microscopy," Nat. Photonics **10**(2), 68–71 (2016).
[23]T. H. Nguyen, C. Edwards, L. L. Goddard, and G. Popescu, "Quantitative phase imaging with partially coherent illumination," Opt. Lett. **39**(19), 5511 (2014).
[24]T. Slabý, P. Kolman, Z. Dostál, M. Antoš, M. Lošťák, and R. Chmelík, "Off-axis setup taking full advantage of incoherent illumination in coherence-controlled holographic microscope," Opt. Express **21**(12), 14747 (2013).
[25]V. Kollarova, J. Collakova, Z. Dostal, P. Vesely, and R. Chmelik, "Quantitative phase imaging through scattering media by means of coherence-controlled holographic microscope," J. Biomed. Opt. **20**(11), 111206 (2015).
[26]A. Dogariu and G. Popescu, "Measuring the phase of spatially coherent polychromatic fields," Phys. Rev. Lett. **89**(24), 243902 (2002).
[27]Z. Wang and G. Popescu, "Quantitative phase imaging with broadband fields," Appl. Phys. Lett. **96**(5), 51117 (2010).
[28]P. Bouchal, R. Chmelík, and Z. Bouchal, "Phase of white light and its compatibility to the optical path," Opt. Express **29**(8), 12398 (2021).
[29]S. B. Mehta and C. J. R. Sheppard, "Using the phase-space imager to analyze partially coherent imaging systems: Bright-field, phase contrast, differential interference contrast, differential phase contrast, and spiral phase contrast," J. Mod. Opt. **57**(9), 718–739 (2010).
[30]S. B. Mehta and C. J. R. Sheppard, "Partially coherent microscope in phase space," J. Opt. Soc. Am. A **35**(8), 1272 (2018).
[31]N. Streibl, "Three-dimensional imaging by a microscope," J. Opt. Soc. Am. A **2**(2), 121 (1985).
[32]R. Chmelik, M. Slaba, V. Kollarova, T. Slaby, M. Lostak, J. Collakova, and Z. Dostal, "The role of coherence in image formation in holographic microscopy," Prog. Opt. **59**, 267–335 (2014).
[33]A. Doblas, E. Sánchez-Ortiga, M. Martínez-Corral, G. Saavedra, P. Andrés, and J. Garcia-Sucerquia, "Shift-variant digital holographic microscopy: Inaccuracies in quantitative phase imaging," Opt. Lett. **38**(8), 1352 (2013).
[34]D. Bouchet, J. Dong, D. Maestre, and T. Juffmann, "Fundamental bounds on the precision of classical phase microscopes," Phys. Rev. Appl. **15**(2), 024047 (2021).
[35]V. Micó, Z. Zalevsky, C. Ferreira, and J. García, "Superresolution digital holographic microscopy for three-dimensional samples," Opt. Express **16**(23), 19260 (2008).
[36]Y. Cotte, F. Toy, P. Jourdain, N. Pavillon, D. Boss, P. Magistretti, P. Marquet, and C. Depeursinge, "Marker-free phase nanoscopy," Nat. Photonics **7**(2), 113–117 (2013).
[37]S. K. Mirsky and N. T. Shaked, "First experimental realization of six-pack holography and its application to dynamic synthetic aperture superresolution," Opt. Express **27**(19), 26708 (2019).
[38]M. Ďuriš, P. Bouchal, K. Rovenská, and R. Chmelík, "Coherence-encoded synthetic aperture for super-resolution quantitative phase imaging," APL Photonics **7**(4), 46105 (2022).
[39]M. Ďuriš, P. Bouchal, and R. Chmelík, "Single-shot super-resolution quantitative phase imaging allowed by coherence gate shaping," APL Photonics **8**(4), 046103 (2023).
[40]J. Di, J. Wu, K. Wang, J. Tang, Y. Li, and J. Zhao, "Quantitative phase imaging using deep learning-based holographic microscope," Front. Phys. **9**, 651313 (2021).
[41]Z. Wang, H. Ding, R. Bashir, G. Popescu, L. Millet, M. Gillette, and V. Chan, "Label-free intracellular transport measured by spatial light interference microscopy," J. Biomed. Opt. **16**(02), 026019 (2011).
[42]S. Pradeep and T. A. Zangle, "LVING reveals the intracellular structure of cell growth," Sci. Rep. **14**(1), 8544 (2024).
[43]Y. Rivenson, T. Liu, Z. Wei, Y. Zhang, K. de Haan, and A. Ozcan, "PhaseStain: The digital staining of label-free quantitative phase microscopy images using deep learning," Light: Sci. Appl. **8**(1), 23 (2019).
[44]D. Pirone, V. Bianco, L. Miccio, P. Memmolo, D. Psaltis, and P. Ferraro, "Beyond fluorescence: Advances in computational label-free full specificity in 3D quantitative phase microscopy," Curr. Opin. Biotechnol. **85**, 103054 (2024).
[45]C. Park, S. Shin, and Y. Park, "Generalized quantification of three-dimensional resolution in optical diffraction tomography using the projection of maximal spatial bandwidths," J. Opt. Soc. Am. A **35**(11), 1891 (2018).